

## Thermoacoustic contrast of prostate cancer due to heating by very high frequency irradiation

This content has been downloaded from IOPscience. Please scroll down to see the full text.

2015 Phys. Med. Biol. 60 689

(<http://iopscience.iop.org/0031-9155/60/2/689>)

View [the table of contents for this issue](#), or go to the [journal homepage](#) for more

Download details:

IP Address: 128.104.46.196

This content was downloaded on 03/01/2015 at 17:16

Please note that [terms and conditions apply](#).

# Thermoacoustic contrast of prostate cancer due to heating by very high frequency irradiation

S K Patch<sup>1</sup>, D Hull<sup>2</sup>, M Thomas<sup>3</sup>, SK Griep<sup>4</sup>, K Jacobsohn<sup>3</sup>  
and WA See<sup>3</sup>

<sup>1</sup> Department of Physics, UW-Milwaukee, 1900 E. Kenwood Blvd., Milwaukee, WI 53211, USA

<sup>2</sup> Bostwick Laboratories, Inc., 4355 Innslake Dr., Glen Allen, VA 23060, USA

<sup>3</sup> Department of Urology, Medical College of Wisconsin, 8700 Wisconsin Ave., Milwaukee WI 53226, USA

<sup>4</sup> Department of Biological Sciences, USC, Allan Hancock Foundation Building, Los Angeles, CA 90089, USA

Received 17 April 2014, revised 3 September 2014

Accepted for publication 20 October 2014

Published 2 January 2015



CrossMark

## Abstract

Applying the thermoacoustic (TA) effect to diagnostic imaging was first proposed in the 1980s. The object under test is irradiated by high-power pulses of electromagnetic energy, which heat tissue and cause thermal expansion. Outgoing TA pressure pulses are detected by ultrasound transducers and reconstructed to provide images of the object. The TA contrast mechanism is strongly dependent upon the frequency of the irradiating electromagnetic pulse.

When very high frequency (VHF) electromagnetic irradiation is utilized, TA signal production is driven by ionic content. Prostatic fluids contain high levels of ionic metabolites, including citrate, zinc, calcium, and magnesium. Healthy prostate glands produce more ionic metabolites than diseased glands. VHF pulses are therefore expected to generate stronger TA signal in healthy prostate glands than in diseased glands.

A benchtop system for performing *ex vivo* TA computed tomography with VHF energy is described and images are presented. The system utilizes irradiation pulses of 700 ns duration exceeding 20 kW power. Reconstructions frequently visualize anatomic landmarks such as the urethra and verumontanum. TA reconstructions from three freshly excised human prostate glands with little, moderate, and severe cancerous involvement are compared with histology. TA signal strength is negatively correlated with percent cancerous involvement in this small sample size. For the 45 regions of interest analyzed, a reconstruction value of 0.4 mV provides 100%

sensitivity but only 29% specificity. This sample size is far too small to draw sweeping conclusions, but the results warrant a larger volume study including comparison of TA images to the gold standard, histology.

Keywords: thermoacoustics, nondestructive (ultrasound/photoacoustic) testing, radiofrequency fields effects, biomedical imaging, cancer, ultrasound imaging

(Some figures may appear in colour only in the online journal)

### List of Acronyms

|       |  |
|-------|--|
| BPH   | benign prostatic hyperplasia                   |
| EPE   | extraprostatic extension                       |
| EM    | electromagnetic imaging                        |
| EMI   | electromagnetic interference                   |
| HGpin | high-grade prostatic intraepithelial neoplasia |
| INFL  | inflammation                                   |
| MRI   | magnetic resonance imaging                     |
| MRSI  | magnetic resonance spectroscopic imaging       |
| PC    | aprostate cancer                               |
| PSA   | prostate-specific antigen                      |
| PSD   | power spectral density                         |
| PZ    | peripheral zone                                |
| ROI   | region of interest                             |
| TA    | thermoacoustic                                 |
| TCT   | thermoacoustic computerized tomography         |
| UHF   | ultra high frequency                           |
| UWB   | ultra wideband                                 |
| VHF   | very high frequency                            |

## 1. Introduction

AG Bell observed the thermoacoustic (TA) effect over a century ago, and application to diagnostic imaging was proposed in the 1980s (Bowen 1981, Bowen *et al* 1981, Caspers and Conway 1982, Nasoni *et al* 1984). TA imaging is a hybrid technique that relies upon conversion of electromagnetic (EM) energy into mechanical energy via thermal expansion to create TA pressure pulses. TA imaging combines the high contrast of dielectric properties with the resolution of ultrasound, providing superior reconstruction stability and resolution over EM imaging and electric impedance tomography techniques. We have developed a benchtop TA computed tomography (TCT) system for studying the clinical utility of TA contrast mechanism generated by very high frequency (VHF) EM irradiation. This system is optimized for imaging small tissue specimens with diameter 6 cm or less, such as the human prostate.

Prostate cancer (PCa) is one of the most challenging cancers for clinical diagnostic imaging techniques. Currently, PCa detection begins with a prostate specific antigen (PSA) blood test and digital rectal examination of the prostate. Multi-parametric MRI of the prostate is an active area of research, but is not yet widely accepted for prostate cancer staging (NCCN 2015). Systematic biopsy (Zukotynski and Haider 2013) and surgical resection of the entire prostate are current standards of care. In contrast, breast cancer biopsies and

lumpectomies based upon mammography images are focal and spare healthy tissue. In summary, neither PCa staging, treatment response nor active surveillance can currently be performed by current diagnostic imaging techniques alone (Outwater and Montilla-Soler 2013).

Unfortunately, these deficiencies in diagnostic imaging affect a large volume of PCa patients. Current annual expectations are for nearly a quarter of a million PCa diagnoses in the United States alone (Society 2013) and over 300 000 deaths worldwide (Ferlay *et al* 2012).

Diagnostic techniques are not limited to imaging. Until the advent of the PSA test the primary method of diagnosis was palpation, to qualitatively assess tissue stiffness. PSA testing was approved by the US Food and Drug Administration in 1994 but received a 'D' rating from the US Preventative Services Task Force in 2012 (Moyer 2012). For several decades it has been understood that prostatic fluids contain high levels of citrate, zinc, calcium, magnesium, and other metabolites which are positively correlated to each other (Kavanagh 1985). Healthy prostate glands produce fluid with threefold higher ionic content than blood and plasma, whereas diseased glands produce prostatic fluid that is similar in conductivity to blood. In particular, numerous studies have established that PCa suppresses citrate and zinc in the peripheral zone (PZ) as reported in the review article (Costello and Franklin 2009). PCa detection by *in vitro* nuclear magnetic resonance spectroscopy of expressed prostatic fluid yielded an area under the receiver operator characteristic curve of 0.89 (Serkova *et al* 2008). Unfortunately, neither PSA nor *in vitro* spectroscopic metabolite detection provides spatial localization of tumors within the prostate.

### 1.1. Current PCa imaging techniques

B-mode ultrasound imaging is typically relegated to merely defining the prostate boundary because acoustic properties of healthy and cancerous prostate tissue are well matched, so image contrast between them is poor. Biopsy of the prostate is required for histologic verification of the PCa diagnosis as well as assessment of disease aggressiveness. Ultrasound is used for systematic biopsy needle placement rather than cancer detection. Imaging to identify disease extent is typically performed only after histologic confirmation, and in most cases is limited to patients whose PCa is suspected to extend beyond the prostate gland but is not yet metastatic. Contrast enhanced ultrasound and manual compression ultrasound elastography used together increased the positive predictive value of cancer detection from 65.1 to 89.7% (Brock *et al* 2012). Elastography visualizes tissue stiffness and can be implemented via many methods reviewed in (Parker *et al* 2011). Operator dependence has limited clinical utility of manual compression elastography, however. Mechanical production of shear waves minimizes operator dependence of shear wave elastography. Good sensitivity and specificity have been reported (Ahmad *et al* 2013), although false positives were found in regions of calcification (Barr *et al* 2012).

Magnetic resonance imaging (MRI) results vary wildly, based upon MRI technique, magnet field strength, choice of receive coils and reader experience (Rooij *et al* 2014). Magnetic resonance spectroscopic imaging (MRSI) provides spatial localization of citrate and other metabolites. Two decades have past since MRSI was first applied to PCa imaging (Narayan and Kurhanewicz 1992) and scores of prostate MRSI papers have followed. Unlike *in vitro* spectroscopy, MRSI only provides only relative levels of metabolites and cannot quantify metabolite concentrations. Additionally, crosstalk between spectral peaks is problematic. A meta-analysis performed in 2008 found little evidence to recommend clinical adoption of MRSI for diagnosis or targeted biopsy (Umbehr *et al* 2009), and more recently a cost-benefit meta-analysis performed in the United Kingdom found expected incremental life years of no more than 0.006 years due to any type of MR-guided biopsy over ultrasound guidance (Mowatt *et al* 2013). More recently, good sensitivity (96.4%) but terrible specificity (7.6%) were reported in a MRI-ultrasound fusion guided prostate biopsy study (Salami *et al* 2014).

fraught with selection and detection bias (Warlick 2014). Clinical practice guidelines issued by both the European Association of Urology and the USA's National Comprehensive Cancer Network withhold recommendation pending validation in clinical trials for image guided biopsy (Eberhardt *et al* 2013, EAU 2014, NCCN 2014). Multi-parametric MRI has also been proposed for confirming eligibility for active surveillance (Stamatakis *et al* 2013) but the American College of Radiology withholds recommendation (Eberhardt *et al* 2013).

In summary, no imaging method has gained widespread acceptance for PCa imaging.

### 1.2. TA contrast mechanism as a function of EM irradiation frequency

The TA contrast mechanism is a complicated function of thermal, mechanical, and dielectric tissue properties. It relies upon conversion of EM energy into mechanical energy. First, EM energy must penetrate into tissue so that absorption of EM energy causes sufficient tissue heating and thermal expansion to generate an outgoing pressure pulse. Therefore, both EM and acoustic attenuation limit depth penetration. Neglecting acoustic attenuation, TA signals are governed by the acoustic wave equation

$$p_{tt}(\mathbf{x}, t) - v_s^2 \Delta p(\mathbf{x}, t) = \frac{\partial}{\partial t} S(\mathbf{x}, t) \quad (1)$$

where  $v_s$  represents sound speed and  $S(\mathbf{x}, t)$  is the TA source.

The TA contrast mechanism driven by VHF irradiation differs from that of photo- and microwave-induced contrast. Optical pulses used for photoacoustics heat proportionally to hemoglobin content and have the ability to discriminate between oxy- and de-oxy hemoglobin. Microwaves heat pure water efficiently, whereas VHF irradiation heats proportionally to ionic content. In the VHF regime, the source term is driven by electrical conductivity. VHF heating with good spatial uniformity permits simplification of the source term in equation (1) to

$$S(\mathbf{x}, t) = E_0^2 \Gamma(\mathbf{x}) \sigma(\mathbf{x}) I(t) \quad (2)$$

where  $E_0$  represents the known amplitude of the electric field,  $I(t)$  is the temporal envelope of the irradiation pulse.  $\sigma(\mathbf{x})$  is electrical conductivity,  $\Gamma(\mathbf{x}) = \beta v_s^2 / C$  is the dimensionless Gruneisen where  $\beta$  and  $C$  represent thermal expansion coefficient and specific heat capacity, respectively. An ideal system would irradiate impulsively so that  $I(t) = \delta(t)$ , making the source term a function of  $\mathbf{x}$  alone,

$$S(\mathbf{x}) = E_0^2 \Gamma(\mathbf{x}) \sigma(\mathbf{x}) \quad (3)$$

The TA source term is therefore the product of applied electric field strength with two tissue parameters, the Gruneisen and electrical conductivity. TA pressures can be written in terms of spherical means of  $S$

$$p(\mathbf{x}, t) = M[S](\mathbf{x}, v_s, t) \quad (4)$$

where  $M$  is the mean value operator, taking the spherical mean of  $S$  over a sphere of radius  $v_s t$  centered at point  $\mathbf{x}$ . TCT images of the source term,  $S$ , are reconstructed tomographically from measurements of the pressure at points  $\mathbf{x}$  on a measurement aperture surrounding the region of interest. Bandlimiting of the TA pulses by the irradiation pulse envelope,  $I$ , can be analyzed analytically (John 1981) or numerically (Lou *et al* 2011). Ultrasound receivers further bandlimit measurements. These effects bandlimit tomographically reconstructed images commensurately (Anastasio *et al* 2007). The pulse envelope and power spectral density (PSD) which bandlimits TA pulses generated in our experimental system are shown in figure 1. Voltages are measured using a line section (Bird 4715) outfitted with 50 dB attenuating slugs (Bird 4274).

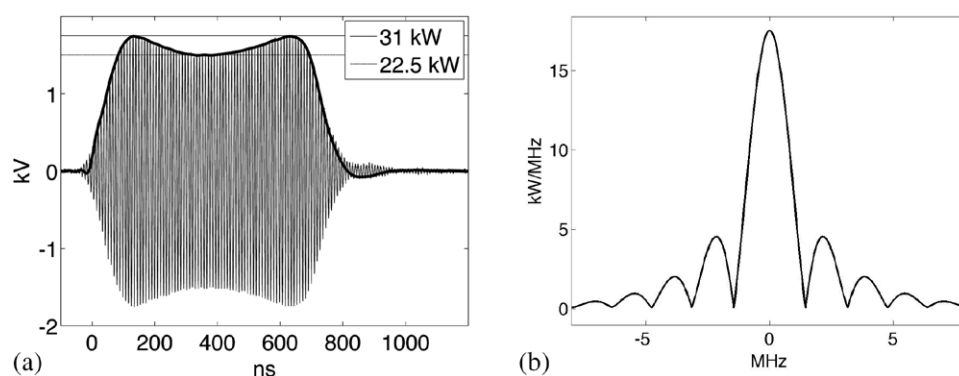


**Figure 1.** (a) 700 ns AC irradiation pulse (thin) and pulse envelope,  $I$  (thick). (b) PSD.

The voltage plotted in figure 1(a) accounts for attenuation. This data is used to compute the PSD plotted in figure 1(b).

### 1.3. TA bandwidth and depth penetration as a function of EM irradiation frequency

In practice, irradiation pulsewidth tends to decrease with irradiation frequency because ultra-wideband (UWB) irradiation is difficult to achieve and efficiently utilize. Short pulses used in photoacoustics approximate a  $\delta$ -function well, as do UWB pulses. 10 ns pulsewidths with VHF (Razansky *et al* 2010) and microwave (Lou *et al* 2012) center frequencies correspond to a PSD with essential bandlimit of 100 MHz. Numerical investigation of even shorter UWB pulses indicates poor depth penetration of the EM field and initial pressure distribution (Tao *et al* 2006). Even if extremely broadband TA pulses can be generated deep in soft tissue, acoustic attenuation will suppress high frequencies in the TA pulses. Clinical ultrasound systems are therefore optimized over the 1–15 MHz regime. Ideally, TA pulse generation would match the clinical regime by irradiating with pulse widths of approximately 65 ns. Unfortunately, current state of the art in TA imaging pulse widths are either below 10 ns or else exceed 300 ns in the microwave regime, 500 ns in the ultra high frequency (UHF) regime, and 700 ns VHF pulses as utilized below. Even the 300 ns microwave pulse widths bandlimit TA pulses to 3.3 MHz, which is at the low end of the clinical US frequency range.

EM frequency affects the source term in many ways including depth penetration and uniformity of EM deposition. Optical depth penetration is only 5.7 mm (Wang and Wu 2007), whereas microwave depth penetration extends to a few cm (Yan *et al* 2005, Tao *et al* 2006, Wang *et al* 2012). Optical fluence decreases smoothly with distance from the laser source, whereas microwaves suffer diffraction and develop standing waves which can cause signal drop-out in microwave induced TCT systems (Li *et al* 2008). 9.4 GHz irradiation has produced A-line TA imaging of thin specimens (Wang *et al* 1999) and 5.66 GHz irradiation has produced a projection image (Olsen and Lin 1983). Nevertheless, foreign objects with low ultrasound contrast were detected *in vivo* in a mouse model using both 6 and 1.2 GHz (Nie *et al* 2009), although the 6 GHz irradiation provided less depth penetration than 1.2 GHz. 6 GHz irradiation was used to study samples of dimension no more than 15 mm (Lou and Xing 2010). Promising images of specimens less than 5 cm in diameter have been obtained using 3 GHz microwave radiation (Ku and Wang 2001, Xu and Wang 2002, Jin *et al* 2005). 1.2 GHz irradiation has produced encouraging *ex vivo* results for detecting breast tumors (Nie *et al* 2008)

and renal calculi (Cao *et al* 2010). UHF radiation at 434 MHz provides sufficient penetration depth to penetrate adipose breast tissue with adequate uniformity for *in vivo* TCT (Kruger *et al* 2000). However, imaging large internal organs may require irradiating with frequencies in the VHF regime of 30–300 MHz, which provides superior depth penetration and uniformity. 7.0 T MRI systems that propagate 300 MHz successfully image the adult head but struggle to provide adequate field uniformity in the abdomen. Body coils in 1.5 and 3.0 T MRI scanners propagate circularly polarized EM energy with carrier frequencies 64 and 128 MHz into large patients with excellent homogeneity and depth penetration. The price exacted for large field of view TA imaging by VHF irradiation is weak TA signal generation.

#### 1.4. Application to PCa imaging

PCa is a compelling application for TA imaging. The well-matched mechanical properties that hinder B-mode ultrasonic imaging of PCa simplifies image reconstruction because we can safely assume constant sound speed. Additionally, preliminary measurements of specific heat capacity,  $C$ , did not differentiate healthy from diseased prostatic tissue at body temperature (Patch *et al* 2011). Therefore, we assume that only the thermal expansion coefficient,  $\beta$ , and EM energy loss drive the TA contrast mechanism in the prostate. Several groups have applied photoacoustic imaging to studies of brachytherapy seeds in tissue phantoms (Harrison and Zemp 2011, Su *et al* 2011, Kuo *et al* 2012). Poor depth penetration of optical radiation may require transurethral light delivery and highly optimized reconstruction (Lediju Bell *et al* 2013), however. *In vivo* studies of the canine prostate have also been performed (Patterson *et al* 2010, Wang *et al* 2010). Multispectral *ex vivo* photoacoustic images of 3–5 mm thick fresh human prostatic tissue performed immediately after gross sectioning could discriminate PCa from healthy prostatic tissue and also from benign prostatic hyperplasia (BPH) based upon deoxyhemoglobin content (Dogra *et al* 2013).

PCa may be particularly well suited to TA imaging using VHF heating which is driven by ionic content. Extremely high levels of citrate in prostatic fluid cause other ions to accommodate and restore electrochemical balance (Kavanagh *et al* 1982). Ionic content of prostatic fluids produced in a healthy gland is approximately three times that of plasma and blood. PCa suppresses citrate, and therefore overall ionic content of prostatic fluids. This relationship applies also to tissue in the PZ where most prostatic fluid is produced and most PCa tumors develop (Costello and Franklin 2009). The central zone is neither a site of significant prostatic fluid production nor high incidence of PCa. BPH frequently arises in the central zone, and elevates citrate and zinc levels to that found in healthy PZ tissue. *In vitro* assays of expressed prostatic fluids can therefore differentiate between the presence of BPH and PCa (Kumar *et al* 2013), but cannot localize tumors within the prostate. TA imaging offers the possibility of localizing tumors, as well as differentiating BPH from cancer. TA image values in the central zone exceeding that expected from normal plasma should indicate the presence of BPH, whereas in the PZ TA image values comparable to plasma are expected to indicate PCa.

To study the TA contrast mechanism in specimens with diameter less than 6 cm, a benchtop imaging system has been optimized for *ex vivo* imaging. We present preliminary results comparing TCT images to the gold standard, histology slides.

## 2. Materials and methods

*Ex vivo* TCT was performed much as described in (Eckhart *et al* 2011, Roggenbuck *et al* 2013b), but in a benchtop imaging system optimized for imaging smaller tissue specimens

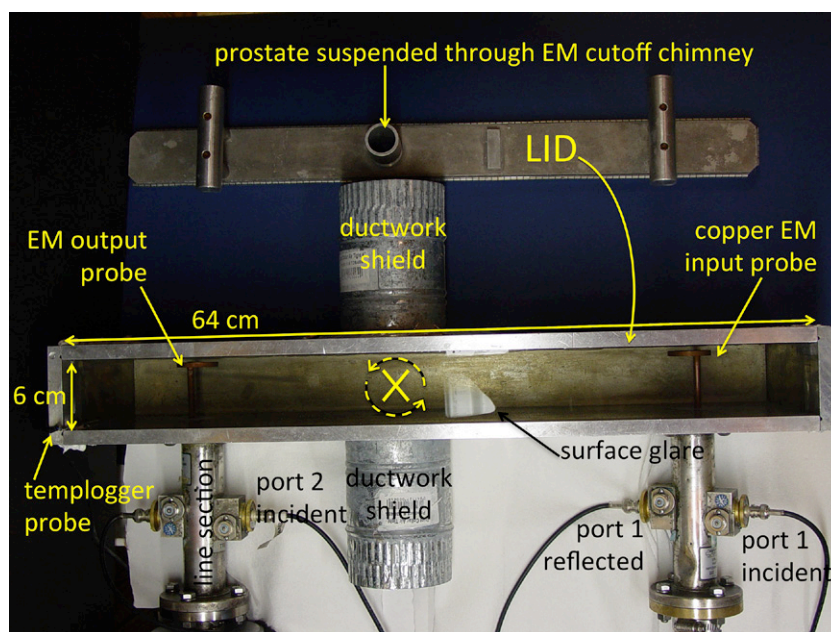


**Figure 2.** Aerial view of benchtop imaging testbed. 'X' indicates the gantry axis of rotation and translation.

(figure 2). The testbed has dimensions of a TE<sub>103</sub> cavity, but with well-matched coupling irises at input and output ports, allowing efficient transmission of a TE<sub>10</sub> pulse through the testbed to a load (Fallon *et al* 2009). The system operates in transmission mode, with EM propagation direction perpendicular to the axial direction of the receive transducers as depicted in figure 3. For imaging small specimens, such as human prostates, the testbed cross section was reduced to 6 cm × 19 cm, concentrating the electric field and generating stronger TA pulses. Additionally, reducing the testbed width from 10 to 6 cm allowed the transducers to be positioned closer to the specimen, increasing signal to noise ratio of the TA measurements. EM parameters were optimized for this smaller benchtop system. The EM irradiation pulse width was reduced to 700 ns, increasing the essential band-limit of TA pressures to 1.4 MHz. Incident and reflected voltages were measured at both input and output ports of the testbed to monitor EM performance of the system. The custom EM amplifier (QEI, VHF50KP), line sections and rigid copper coaxial connections (EIA 1 5/8 inches) remained unchanged from our previous work. A digital oscilloscope (Tektronix DPO7104) with onboard personal computer acquired both EM and TCT data. The scan process was driven by LabView software running on the oscilloscope. The EM amplifier and testbed were enclosed in a 100 dB Faraday cage (ETS Lindgren) outfitted with a penetration panel containing coaxial connectors for data lines as well as one USB connector for a communication line as depicted in figure 4.

### 2.1. EM power measurements

To control for systematic variations in TA signal strength due to amplifier power output, incident and reflected power at both input and output ports of the testbed was monitored by recording voltages on a four-channel digital oscilloscope set to 1 GHz bandwidth and 200 ps

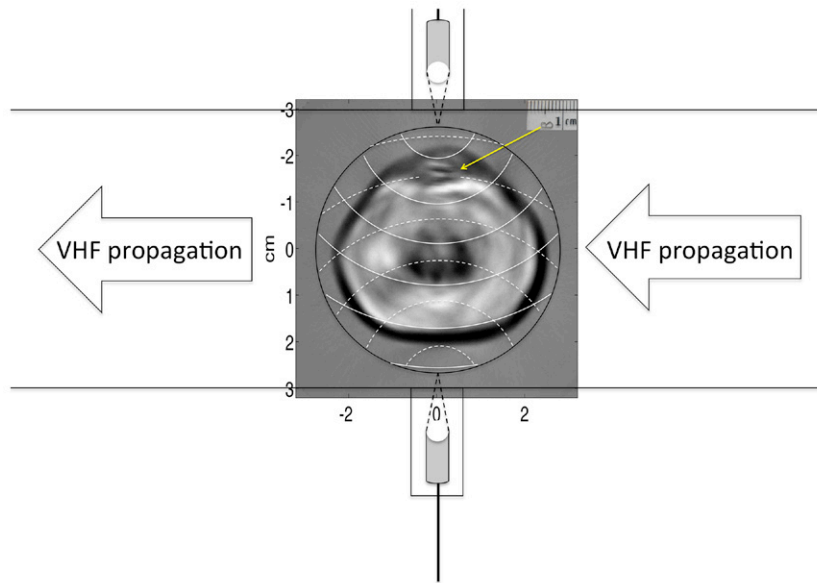


**Figure 3.** TCT data acquisition geometry. Black solid circle indicates the ultrasound receiver trajectory relative to the specimen. VHF irradiation pulse propagates perpendicular to the axes of the transducers. Thin white circles indicate the surface of spherical integrals measured by upper (solid) and lower (dashed) transducers.

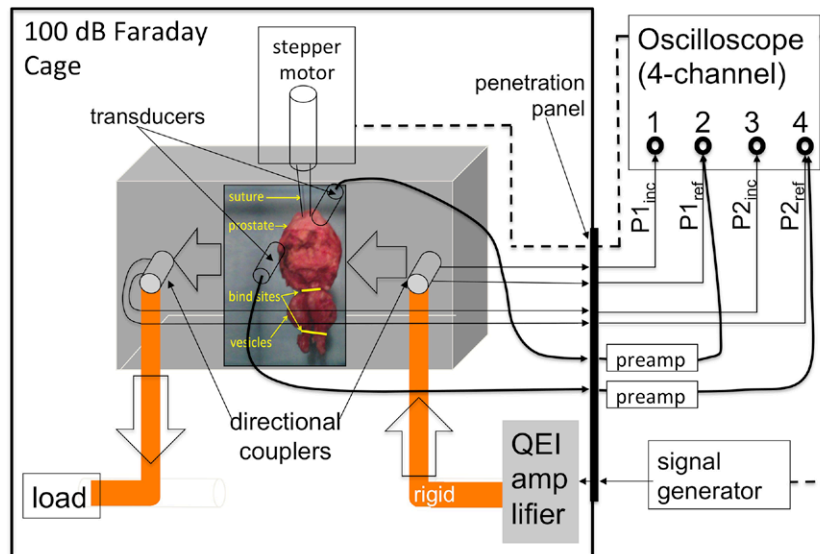


**Figure 4.** Schematic of TCT system. Thick solid indicates TA data lines. Thin solid indicates low power VHF data lines. Hollow arrows indicate high-power VHF pulse. Thick dashed indicates communication lines between LabView, signal generator, and stepper motor.

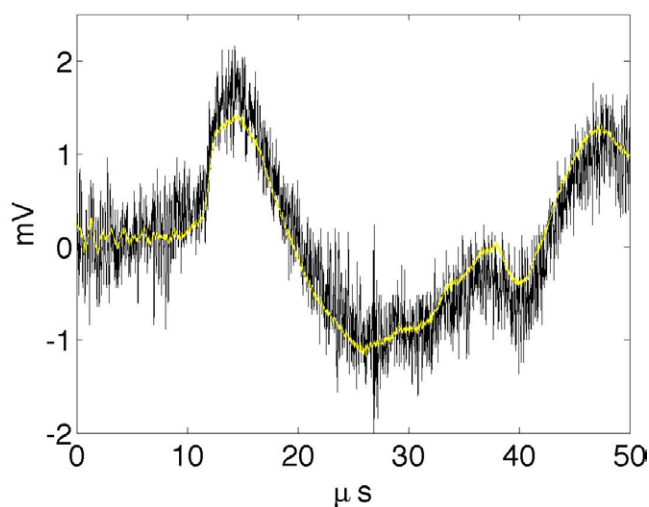


**Figure 5.** TA pulses as displayed on and recorded by oscilloscope. Single realization in thin black, average of 64 pulses in thick yellow.

sampling rate. A pulse incident upon the input port is shown in figure 1 (left). Four-channel control data taken immediately before and/or after loading the testbed with a prostate recorded both incident and reflected voltages at each port. During TA data acquisition, however, two channels were used to record TA pulses. The remaining two channels were used to monitor incident power at input and output ports. Voltages were measured between acquisitions of single-slice TA sinograms. Twenty-four realizations were acquired for each control measurement, and six realizations were acquired between TA sinograms.

## 2.2. TCT data acquisition

To improve stability of the tomographic gantry the testbed design was rotated from that described in (Eckhart *et al* 2011). Specimens were suspended below a dual motion stepper motor (Haydon Kerk) by a stiff monofilament surgical suture, ensuring a stable vertical axis of rotation and translation. Spatial encoding was obtained by rotating and translating the specimen in step-and-shoot mode. The translation increment was 3 mm, consistent with the 3 mm distance between histology levels. Image planes were acquired from apex to base. The rotation increment was  $1.8^\circ$  between tomographic views. To avoid ‘jerking’ the specimen, 64 subrotations were each followed by a 25 ms delay. After rotating the full  $1.8^\circ$  increment another 500 ms delay allowed the specimen to come to rest before data acquisition commenced. The EM pulse repetition frequency was 100 Hz and 64 TA pulses were averaged to suppress noise as depicted in figure 5. For each tomographic view, more than 2 s were required for specimen repositioning, whereas data acquisition required less than 1 s. Saving data to disk and communication within LabView required additional time, so total dwell time at each tomographic view was approximately 5 s. Partial-scan TCT sinograms, typically containing only 140 of 200 views, were acquired by each transducer over a period of approximately 12 min per acquisition slice. To minimize specimen heating, duty cycle was minimized by irradiating only during data acquisition. EM irradiation was not applied during specimen positioning, LabView communication, and saving data to disk.

Two identical 2.25 MHz focused single-element transducers with 0.5 inches diameter and 0.8 inches distance to focus (Olympus V306) were positioned on opposite sides of the specimen. The acoustic couplant was deionized water mixed with a concentration of 15 g L<sup>-1</sup> glycine powder. Glycine powder was added to minimize water absorption by the tissue, which would impair histologic analysis. Glycine powder did not affect speed of sound or attenuation as measured during system validation. TA pulses were amplified 54 dB by a low noise preamplifier (Olympus 5662) positioned outside of the Faraday cage to shield it from EM interference (EMI). Sensitivity of similar transducers amplified by only 40 dB was approximately 1 mV Pa<sup>-1</sup> (Pachauri *et al* 2008), corresponding to 5 mV Pa<sup>-1</sup> when amplified by 54 dB. Averaged TA pulses like that plotted with the thick line in figure 5 were written to disk by the digital oscilloscope. Bandwidth and sampling rate were lowered to the lowest available settings compatible with both LabView and TekTronix software, 20 MHz and 10 ns.

The focus of each transducer was treated as a point receiver (Li *et al* 2006), acquiring circular integrals of the source term,  $S(\mathbf{x})$ , as depicted by thin white lines in figure 3. Data from the transducers was carried by doubly-shielded coaxial cables, which were additionally shielded using commercial aluminum ductwork. Coaxial cables and aluminum ductwork were grounded at the penetration panel.

This acquisition system is less costly and more sensitive than clinical ultrasound transducers with element diameter less than 1 mm, but suffers from two drawbacks. It is sensitive to EMI and acquisition using only two single element transducers requires lengthy scan times. To shield the transducers from the EM irradiation pulse, transducers were recessed 1 cm inside cutoff chimneys, so that the focus protruded approximately 5 mm into the testbed volume, as depicted in figure 3. Prostate tissue degrades slowly after excision and is therefore suitable for studies of the fundamental contrast mechanism in benchtop systems with lengthy scan times, in particular when the specimens remain chilled (one method to reduce autolysis). Autolysis, readily recognized by light microscopy, was not observed in any of the specimens upon light microscopic examination. It is therefore evident that the cell membranes remained intact. Should the contrast mechanism prove clinically useful in large volume *ex vivo* studies, development of sophisticated clinical prototypes will be warranted.

### 2.3. TCT image reconstruction

Image reconstruction was performed by filtered back projection, with significant data correction applied prior to back projection (Roggenbuck *et al* 2013a). Each TA projection was bandpass filtered with a bandpass of 100 kHz to 5 MHz and then Hilbert transformed. Sinogram-space ‘ringfix’ correction was applied to remove signal due to EMI as shown in figure 6. Acoustic scattering within the prostate is minimal and care was taken to remove signal due to acoustic reflections at the prostate/couplant boundary. EMI causes high-frequency vertical streaks in sinograms and rings in reconstructed images, whereas multiple reflections at the prostate-couplant interface typically create a low frequency ‘halo-effect’ around the boundary of the specimen. Corrected measurements are referred to as  $p_{\text{corr}}$ . Finally, partial-scan TA sinograms were smoothly combined to simulate complete 360° acquisitions by a single transducer. Because the transducers are directional, backprojection was performed in plane, yielding the approximate reconstruction formula

$$S(\mathbf{x}) \sim R \int_{\theta=0}^{2\pi} p_{\text{corr}}(\mathbf{y}, |\mathbf{x} - \mathbf{y}| / \nu_s) \frac{\mathbf{n} \cdot (\mathbf{x} - \mathbf{y})}{|\mathbf{x} - \mathbf{y}|^2} d\mathbf{y} \quad (5)$$

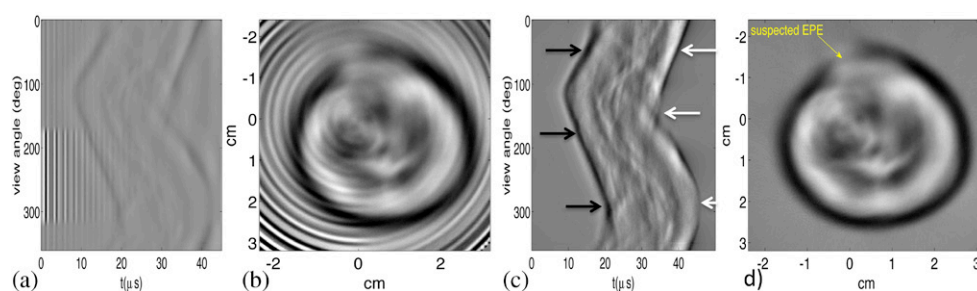


**Figure 6.** Single-element transducer measurements and reconstructions, before and after EMI and multiple reflection corrections. Bandpass filtered sinogram (a) and reconstructed image (b) without correction. (c) Sinogram corrected for EMI and multiple acoustic reflections. Leading compressional edge of the pulse and primary rarefactional region indicated with black and white arrows, respectively. (d) Image reconstructed from corrected sinogram, with site of suspected EPE indicated by yellow arrow.

Here  $y(\theta) = (R \cos \theta, R \sin \theta, z)$  are detector trajectory points where reconstruction point  $x = (x, y, z)$ ,  $R$  is the radius of the acquisition trajectory and  $\mathbf{n}$  is the inward pointing unit normal. In this system  $R \sim 25$  mm because the transducer focus protrudes beyond the sidewall of a 6 cm wide testbed.

#### 2.4. Specimen acquisition and handling

All specimens were from biopsy-confirmed PCa patients who received radical prostatectomy as part of their normal care. Inclusion criteria were preoperative stage T2a, b, c or PSA > 9 or primary Gleason > 3. An additional requirement that the prostate diameter be limited to 6 cm in left–right (LR) and anterior–posterior (AP) directions ensured that each specimen would fit inside the benchtop imaging system. The Institutional Review Board of the Medical College of Wisconsin approved this prospective study. Informed consent was obtained from all subjects.

More than three-dozen specimens were scanned and most were removed by robotic surgical technique. All three of the specimens sent for thorough histologic comparison were removed robotically. During robotic surgery, 3 mm surgical staples were affixed along a ‘staple line’ on the anterior portion of the prostate to control bleeding. After the vascular attachments of the prostate were divided, the prostate and attached seminal vesicles were placed in a plastic bag and remained unperfused inside the warm abdomen for approximately 1 h until completion of the surgical reconstruction. The prostate was then removed from the body and the staple line was removed from the prostate. The remaining specimen was placed in a biohazard bag and packed in wet ice for transport to the benchtop imaging system. Deviations from this procedure included: failure to completely remove the staple line, imaging with 3.5 MHz transducers rather than 2.25 MHz, EM amplifier malfunction, templogger failure and oversized specimen (greater than 6 cm in left–right or anterior–posterior dimension). Although these data sets cannot be included in statistical analysis comparing TA signal production the surgical staples and higher-frequency transducer demonstrate good in-plane resolution.

Care was taken to preserve the fresh prostate tissue specimens for histologic analysis required for patient care. Imaging commenced within 60–90 min and data acquisition was limited to 4 h. Specimens were immersed in acoustic couplant that was chilled to prevent autolysis (cell breakdown occurring after cell death). Temperatures were recorded by a templogger every minute during data acquisition and varied from 3 to 13 °C. Prostate tissue is denser than water, but vesicles

**Table 1.** TCT reconstruction value versus Gleason Scores.

| Specimen | ROI | % cancer | GL score           | % G13 | % G14 | $\mu$ (mV) | $\sigma$ (mV) | $T$ ( $^{\circ}$ C) |
|----------|-----|----------|--------------------|-------|-------|------------|---------------|---------------------|
| 1        | 1   | 80       | 3 + 4              | 90    | 10    | 0.09       | 0.12          | 6.7                 |
|          | 2   | 100      | 4 + 3              | 40    | 60    | 0.13       | 0.12          |                     |
|          | 3   | 10       | <sup>a</sup>       |       |       | 0.07       | 0.09          |                     |
| 2        | 1   | 90       | 3 + 4              | 90    | 10    | 0.22       | 0.08          | 7.6                 |
|          | 2   | 0        |                    |       |       | 0.29       | 0.09          |                     |
|          | 3   | 100      | 4 + 3              | 20    | 80    | 0.27       | 0.08          |                     |
|          | 4   | 0        |                    |       |       | 0.24       | 0.14          |                     |
| 3        | 1   | 30       | 3 + 3 <sup>b</sup> | 100   |       | 0.34       | 0.11          | 11.6                |
|          | 2   | 0        |                    |       |       | 0.49       | 0.13          |                     |
|          | 3   | 0        | cystic             |       |       | 0.52       | 0.14          |                     |
|          | 4   | 0        |                    |       |       | 0.49       | 0.18          |                     |

<sup>a</sup>Less than 10% HGpin, many foci of cystic change associated with acute and chronic inflammation.

<sup>b</sup>Also significant inflammation.

are often buoyant. Therefore, the vesicles were bundled together using small rubber bands as shown in figure 4. A glass bead was often attached to ensure that they would hang directly below the prostate. Immediately after data acquisition specimens were formalin-fixed. The entire prostate was sliced at 3 mm intervals and submitted for diagnostic histological processing.

## 2.5. Histology

Diagnostic pathology reports were available for all specimens. These diagnostic reports provide only percent cancerous involvement averaged throughout the entire gland, largest dimension of largest tumor, and Gleason grade. Diagnostic reports also indicate whether tumor extended beyond the capsule of the prostate (extraprostatic extension (EPE)) or the presence of a positive surgical margin, but do not typically specify location or dimension of the interruption of the prostate capsule. Unfortunately, none of these diagnostic metrics provide spatial information that can be directly correlated to axial TCT reconstructions.

Histology slides from three prostate specimens that generated clear anatomical markers in TCT images were selected for labor-intensive reading and annotation by a fellowship-trained genitourinary pathologist with greater than 6 years experience (David Hull). The specimens selected contained little, moderate, and extensive disease, respectively. Additionally, TCT images of each clearly display the verumontanum. Each cancerous region in histology was assigned a Gleason score, which is the sum of primary and secondary Gleason grades, ranging from 1 (least aggressive) to 5 (most aggressive). The primary Gleason grade represents the Gleason pattern that constitutes the greatest volume of cancer. The secondary Gleason grade corresponds to the second most prevalent Gleason pattern. Primary and secondary Gleason grades in the specimens examined ranged from 3 (least aggressive) to 5 (most aggressive). Due to the variety of PCa treatment options, patients referred for surgery typically present with Gleason scores of 6 or 7. All specimens examined in this study were Gleason score 6 or 7. Regions of inflammation (INFL), atrophy, nodular hyperplasia, high-grade prostatic intraepithelial neoplasia (HGpin) and EPE were also noted. The type of tissue was annotated directly on histology slides as well as on a detailed report form. Descriptions of cancerous regions included percentage of cancer within the region (table 1, 3rd column) and Gleason grade of cancer within the region (column 4). Additionally, the percentage of each Gleason grade contained within the region was provided (columns 5–6).

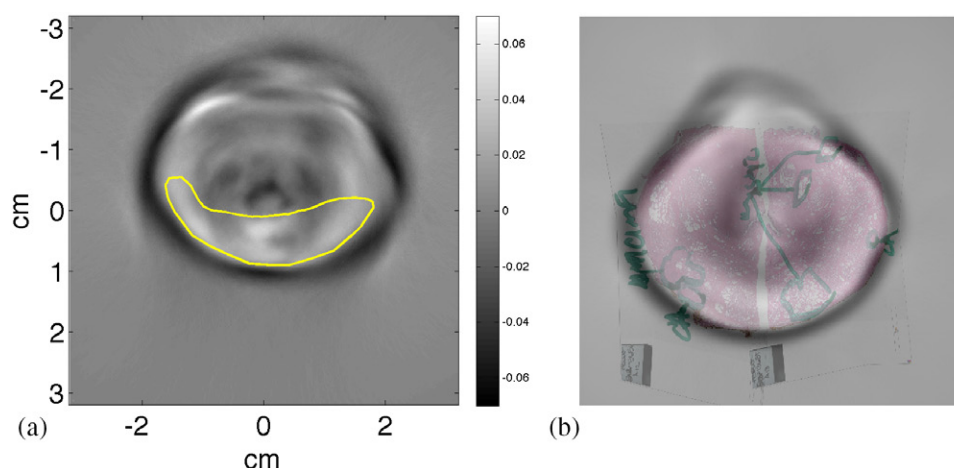


**Figure 7.** Designation of regions of interest. (a) Control specimen marked with single ROI approximating the posterior PZ. (b) Overlay of histology slides onto the corresponding TA image of specimen #3.

TCT reconstruction slices were correlated to histology levels using the wedge-shaped verumontanum as the primary anatomical landmark. Although the step size between histology and TCT reconstruction slices were both 3 mm, the offset between histology and TCT is unknown. Additionally, the fixation process deforms tissue, further confounding correlation between histology and reconstruction slices.

Two types of regions of interest (ROIs) were assigned for two different purposes. The posterior region approximating the entire PZ was annotated as one large ROI on each TCT image slice as shown in figure 7(a). This was performed for specimens for which temperature data was available. *All* prostates in this study contained biopsy-confirmed cancer, but we have access to detailed histologic analysis for only a few specimens. The 25 ‘controls’ are simply specimens for which detailed histology is unavailable. This was done to determine whether temperature fluctuations during the 4 h scan process affect TA signal production.

To determine whether TA signal strength is correlated to disease state, the PZ was divided into regions corresponding to different tissue types noted by the pathologist. TCT imaging of the whole fresh prostate was performed prior to formalin fixation, which can deform tissue. Therefore, TCT images represent the ‘true’ morphology. Regions marked on histology slides were registered to corresponding regions on TCT images using anatomical landmarks as control points. A piecewise linear scheme was used to overlay histology slides upon the TCT reconstructions as shown in figure 7(b). TCT image resolution is low, so only coarse subdivision was performed as shown in figures 8(d–f).

Electric field strength is proportional to voltage and power is proportional to voltage squared. Because the rigid coaxial connections to the testbed were standard  $50\ \Omega$ , power was computed simply by correcting measured voltages for attenuation and then dividing the time averaged voltage squared during each pulse by  $50\ \Omega$ .

### 3. Results

TA image values in select regions of the PZ were correlated to disease state for three histology specimens. Image values averaged throughout the PZ were independent of temperature but weakly dependent on overall cancerous involvement throughout the entire prostate.

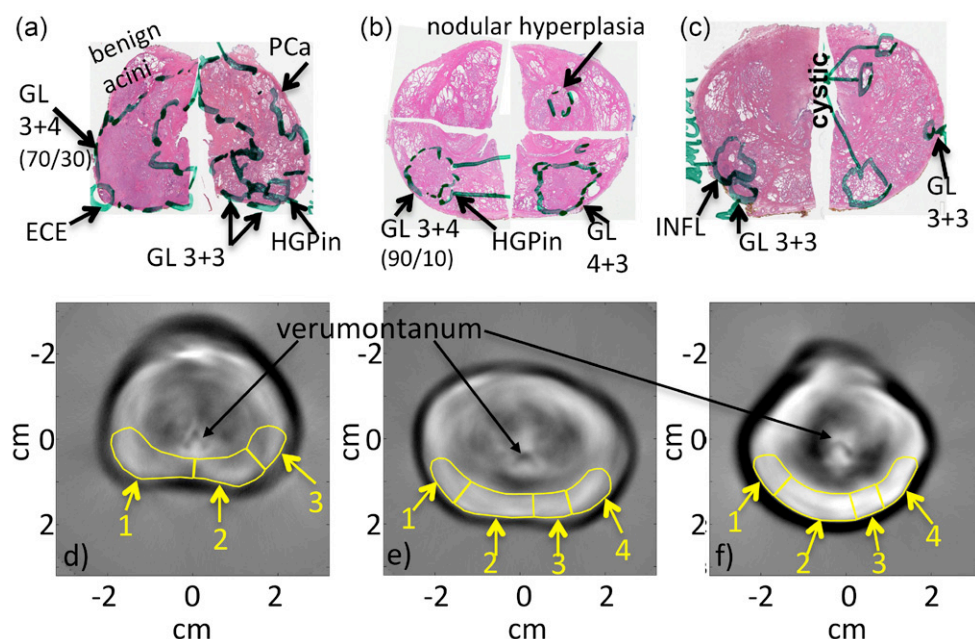


**Figure 8.** TCT reconstructions versus histology slides. ROIs segment the posterior PZ. Display window of TCT images is  $[-0.7 \ 0.7]$  mV. Arrows indicate the verumontanum. (a,d) Specimen #1 suffered approximately 80% involvement. (b,e) Specimen #2 had less than 50% involvement. (c,f) Specimen #3 had minimal cancerous involvement.

### 3.1. TA reconstruction values: correlation with disease status

In reconstructions from specimens 1–3 TA signal strength decreases with tumor involvement. Reconstruction slices that clearly show the verumontanum are compared to histology in figure 8. Regions marked with yellow approximate regions of involvement as annotated on the corresponding histology slide. Results are quantified in table 1. Gleason grade and percent involvement of each grade are listed in columns 4–6. Columns 7 and 8 contain mean ( $\mu$ ) and standard deviation ( $\sigma$ ) of TCT reconstruction values. Because glycine solution has very low electrical conductivity, reconstruction values in the background region outside the prostate should be zero. Large ROIs placed in the background regions have mean reconstruction values of  $5e-3$  mV or less. The least diseased specimen, #3, generated mean reconstruction values of 0.49 mV throughout most of the PZ except for a small region of low-grade cancer, which corresponds to slightly suppressed mean reconstruction value of 0.34 mV. Strongest average reconstruction values from the PZ of the most diseased specimen, #1, were very nearly within one standard deviation of zero at  $0.13 \pm 0.12$  mV.

Average reconstruction values for healthy regions in specimen #3 are four-fold greater than the values for cancerous regions in specimen #1. Forty-five ROIs were analyzed from these three specimens. Within this small sample, using a cut-off value of 0.4 mV would yield perfect sensitivity of  $24/(24 + 0) = 100\%$  but poor specificity of  $6/(6 + 15) = 6/21 = 29\%$  for PCa detection.

### 3.2. TA reconstruction values: temperature dependence

Maintaining thermal control during data acquisition was difficult, not only due to thermal heating of the specimen but also heat emitted by the VHF amplifier. Temperatures fluctuated

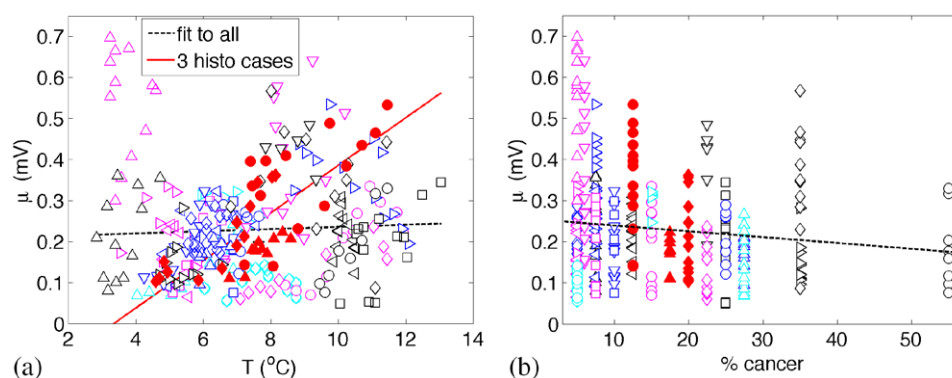


**Figure 9.** Average reconstruction values in posterior PZ. Solid symbols for three selected prostates with extensive, moderate, and minimal disease are diamond, triangle, and circle. Hollow symbols represent 25 control specimens. (a) TA average value versus temperature. (b) TA average value versus overall cancerous involvement.

over a range of  $10^{\circ}\text{C}$ , but were concentrated generally in the  $5\text{--}8^{\circ}\text{C}$  range. Temperatures were recorded during acquisition and correlated to image slice using time stamps on data files (table 1, column 9). Mean reconstruction values from posterior regions approximating the PZs are plotted with respect to testbed temperature during acquisition in figure 9(a). Each different symbol-color combination represents a different prostate. Solid red symbols represent the three prostates selected for thorough histologic annotation. Hollow symbols (black, blue and magenta) represent controls. Linear least squares fits for the three prostates selected for detailed histology (solid red line) as well as the 25 control specimens are plotted (dashed black line). Temperature dependence of the large group of 308 slices from 27 prostates is nearly zero, as the dashed black line is nearly horizontal. Therefore, we conclude that the apparent temperature dependence within the small set of only 37 slices from three specimens is spurious.

### 3.3. TA reconstruction values: dependence upon percent overall cancerous involvement

The same reconstruction values are plotted against overall percent involvement throughout the entire prostate as stated in the clinical pathology report. Therefore, several symbols representing the mean reconstruction values in each of several histology levels are plotted in a vertical line above the overall percent involvement in figure 9(b). A linear fit to these data shows weak dependence on overall percent cancer throughout the prostate.

### 3.4. TA reconstruction values: dependence upon incident EM power

EM power levels computed from measured voltages ranged from 20–25 kW as plotted in figure 10. Error bars represent one standard deviation above and below the mean. Measurements taken when the testbed was loaded with the prostate are plotted between the vertical dashed lines. Measurements taken before or after loading the testbed are plotted to the left and right, respectively. Circles and squares represent incident power at input and output ports, respectively. Diamonds represent reflected power at the input port. Hollow symbols represent two-channel data acquired during TA data acquisition; solid symbols represent four-channel

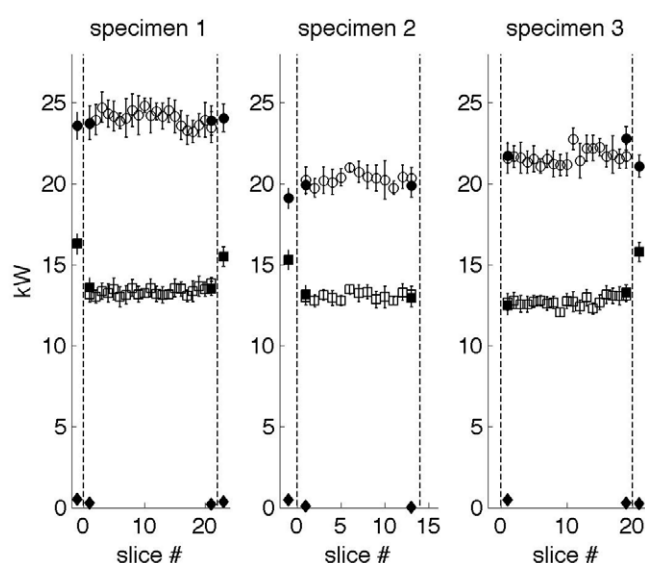


**Figure 10.** EM power measurements. Circles and squares represent incident power at input and output ports, respectively. Diamonds represent reflected power at the input port. Hollow symbols represent two-channel data acquired during TA acquisition; solid symbols represent four-channel control measurements acquired before and after imaging.

control measurements, which include reflected power. Note that these values represent power incident and reflected upon the entire system, glycine dielectric and prostate, rather than an individual reconstruction slice.

#### 4. Discussion

The low-resolution reconstructions presented here hold promise that the contrast mechanism may provide clinically useful information. In the specimens selected for detailed histology, TA signal strength is suppressed in cancerous regions, corroborating conventional wisdom that metabolite production by cancerous glands is suppressed. Reconstructions routinely visualize structures such as the verumontanum mid-gland, as well as the urethra near the apex and base. Despite band-limitations induced by a 700 ns EM irradiation pulse, small ducts were sometimes visible.

Besides the small sample size there are several limitations to this preliminary *ex vivo* study. The 6 cm testbed width restricted our study to prostates of dimension 6 cm or less in both L/R and A/P directions. This may have skewed our pool of specimens, but VHF excitation can easily provide depth penetration sufficient for imaging larger prostates. Loss of prostatic fluid during specimen procurement and imaging is expected to be low. Because specimens were removed robotically, a small amount of prostatic fluid may have been expressed as the prostate was extracted through a small incision. The capsule is designed to protect an organ, and mitigate fluid transport across its boundary. Ionic loss at sites of EPE and positive margins could artificially suppress TA signal generation and future work with a large number of samples should exclude these regions. A lesser concern is lack of blood flow during *ex vivo* imaging. Although the prostate is highly vascular, flow rates are relatively slow and radical prostatectomy specimens retain 'steady state' blood volume within the prostate microvasculature.

Finally, we were forced to keep the specimen chilled to minimize autolysis. Temperature dependence of the parameters comprising the Gruneisen and dielectric properties of water is well understood. Temperature dependence of these parameters for blood and soft tissue is less well understood, but is unlikely to account for the 400% increase in signal generated by specimen #3 over #1. Furthermore, signal produced in the PZ of 25 control specimens was nearly independent of temperature, increasing by less than 20% from 3 to 13 °C. *In vivo* scanning at body temperature should increase TA signal strength somewhat over that generated by the chilled specimens imaged in this study.

The weak dependence of TA reconstruction values upon percent overall cancerous involvement shown in figure 9(b) is encouraging. A correlation is expected, based upon the hypothesis that PCa suppresses ionic content of prostatic fluid. Perfect correlation, however, would indicate that TCT could only identify overall cancerous involvement, but not localize individual tumors.

Although high-power measurements are difficult to make accurately, the results in figure 10 give confidence that weak signal generation by specimen #1 was due to the specimen itself rather than experimental factors. Incident power measurements varied by approximately 20% between the specimens and were greatest for specimen #1, although specimen #1 generated the weakest TA signal. Additionally, these measurements verify good EM system performance. Reflected power was extremely low in all control measurements. Furthermore, loading the testbed with a lossy tissue specimen decreases power transmitted through the testbed, and the power lost within the specimen gives rise to TA signal. Reflected power at the input port often decreases when the testbed is loaded with a specimen. Although some EM power may be reflected at the couplant-tissue interface, lossy specimens often act as power sinks, reducing overall reflected power.

Unlike microwave and optical heating, VHF radiation provides excellent depth penetration. The rarefaction portion of each TA pulse was clearly visible throughout most sinograms, demonstrating that the TA pressures produced were sufficiently strong to propagate through the entire gland.

If more these preliminary results are corroborated by larger studies then development of a working clinical prototype will be warranted.

## Acknowledgments

This project was partially supported by the National Center for Advancing Translational Sciences, National Institutes of Health, through Grant Number 8UL1TR000055. Its contents are solely the responsibility of the authors and do not necessarily represent the official views of the NIH. SKG was supported by UW-Milwaukee's Office of Undergraduate Research.

## References

- Ahmad S, Cao R, Varghese T, Bidaut L and Nabi G 2013 Transrectal quantitative shear wave elastography in the detection and characterisation of prostate cancer *Surg. Endosc.* **27** 3280–7
- Anastasio M, Zhang J, Modgil D and La Rivière P J 2007 Application of inverse source concepts to photoacoustic tomography *Inverse Probl.* **23** S21–36
- Barr R, Memo R and Shaub C 2012 Shear wave ultrasound elastography of the prostate initial results *Ultrasound Q.* **28** 13–20
- Bowen T 1981 Radiation-induced thermoacoustic soft tissue imaging *IEEE Ultrasonics Symp.* pp 817–22
- Bowen T, Nasoni R L, Pifer A E and Sembrosk G H 1981 Some experimental results on the thermoacoustic imaging of tissue equivalent phantom materials *IEEE Ultrasonics Symp.* pp 823–7

- Brock M, Eggert T, Palisaar R, Roghmann F, Braun K, Löttenberg B, Sommerer F, Noldus J and Von Bodman C 2012 Multiparametric ultrasound of the prostate: adding contrast enhanced ultrasound to real-time elastography to detect histopathologically confirmed cancer *J. Urol.* **189** 93–8
- Cao C, Nie L, Lou C and Xing D 2010 The feasibility of using microwave-induced thermoacoustic tomography for detection and evaluation of renal calculi *Phys. Med. Biol.* **55** 5203–12
- Caspers F and Conway J 1982 Measurement of power density in a lossy material by means of electromagnetically induced acoustic signals for non-invasive determination of spatial thermal absorption in connection with pulsed hyperthermia *12th European Microwave Conf. (Helsinki, Finland)*
- Costello L C and Franklin R B 2009 Prostatic fluid electrolyte composition for the screening of prostate cancer: a potential solution to a major problem *Prostate Cancer Prostatic Dis.* **12** 17–24
- Dogra V S, Chinni B K, Valluru K S, Joseph J V, Ghazi A, Yao J L, Evans K, Messing E M and Rao N A 2013 Multispectral photoacoustic imaging of prostate cancer: preliminary *ex-vivo* results *J. Clin. Imaging Sci.* **3** 41
- EAU 2014 The role of imaging *Guidelines on Prostate Cancer* (Arnhem: European Association of Urology)
- Eberhardt S *et al* 2013 ACR appropriateness criteria prostate cancer—pretreatment detection, staging, and surveillance *J. Am. Coll. Radiol.* **10** 83–92
- Eckhart A, Balmer R, See W and Patch S 2011 *Ex vivo* thermoacoustic imaging over large fields of view with 108 MHz irradiation *IEEE Trans. Biomed. Eng.* **58** 2238–46
- Fallon D, Yan L, Hanson G W and Patch S K 2009 RF testbed for thermoacoustic tomography *Rev. Sci. Instrum.* **80** 064301
- Ferlay J, Soerjomataram I, Ervik M, Dikshit R, Eser S, Mathers C, Rebelo M, Parkin D M, Forman D and Bray F 2012 *GLOBOCAN 2012 v1.0, Cancer Incidence and Mortality Worldwide: IARC CancerBase No. 11* (Lyon: International Agency for Research on Cancer)
- Harrison T and Zemp R J 2011 Coregistered photoacoustic-ultrasound imaging applied to brachytherapy *J. Biomed. Opt.* **16** 080502
- Jin X, Xu Y, Wang L V, Fang Y R, Zanelli C I and Howard S M 2005 Imaging of high-intensity focused ultrasound-induced lesions in soft biological tissue using thermoacoustic tomography *Med. Phys.* **32** 5–11
- John F 1981 *Partial Differential Equations* (New York: Springer)
- Kavanagh J P 1985 Sodium, potassium, calcium, magnesium, zinc, citrate and chloride content of human prostatic and seminal fluid *J. Reprod. Fertil.* **75** 35–41
- Kavanagh J P, Darby C and Costello C B 1982 The response of seven prostatic fluid components to prostatic disease *Int. J. Androl.* **5** 487–96
- Kruger R A, Miller K D, Reynolds H E, Kiser W L Jr, Reinecke D R and Kruger G A 2000 Contrast enhancement of breast cancer *in vivo* using thermoacoustic CT at 434 MHz *Radiology* **216** 279–83
- Ku G and Wang L V 2001 Scanning microwave-induced thermoacoustic tomography: signal, resolution, and contrast *Med. Phys.* **28** 4–10
- Kumar V, Dwivedi D K and Jagannathan N R 2013 High-resolution NMR spectroscopy of human body fluids and tissues in relation to prostate cancer *NMR Biomed.* **27** 80–9
- Kuo N, Kang H J, Song D Y, Kang J U and Boctor E M 2012 Real-time photoacoustic imaging of prostate brachytherapy seeds using a clinical ultrasound system *J. Biomed. Opt.* **17** 066005
- Lediju Bell M A, Kuo N, Song D Y and Boctor E M 2013 Short-lag spatial coherence beamforming of photoacoustic images for enhanced visualization of prostate brachytherapy seeds *Biomed. Opt. Express* **4** 1964–77
- Li C, Pramanik M, Ku G and Wang L 2008 Image distortion in thermoacoustic tomography caused by microwave diffraction *Phys. Rev. E* **77** 031923
- Li M-L, Zhang H F, Maslov K, Stoica G and Wang L V 2006 Improved *in vivo* photoacoustic microscopy based on a virtual-detector concept *Opt. Lett.* **31** 474–6
- Lou C, Nie L and Xu D 2011 Effect of excitation pulse width on thermoacoustic signal characteristics and the corresponding algorithm for optimization of imaging resolution *J. Appl. Phys.* **110** 083101
- Lou C and Xing D 2010 Temperature monitoring utilising thermoacoustic signals during pulsed microwave thermotherapy: a feasibility study *Int. J. Hyperthermia* **26** 338–46
- Lou C, Yang S, Ji Z, Chen Q and Xing D 2012 Ultrashort microwave-induced thermoacoustic imaging: a breakthrough in excitation efficiency and spatial resolution *Phys. Rev. Lett.* **109** 218101

- Mowatt G *et al* 2013 The diagnostic accuracy and cost-effectiveness of magnetic resonance spectroscopy and enhanced magnetic resonance imaging techniques in aiding the localisation of prostate abnormalities for biopsy: a systematic review and economic evaluation *Health Technol. Assess.* **17** 1–281
- Moyer V A 2012 Screening for prostate cancer: US Preventive Services Task Force recommendation statement *Ann. Intern. Med.* **157** 120–34
- Narayan P and Kurhanewicz J 1992 Magnetic resonance spectroscopy in prostate disease: diagnostic possibilities and future developments *Prostate Suppl.* **4** 43–50
- Nasoni R L, Evanoff G A, Halverson P G and Bowen T 1984 Thermoacoustic emission by deeply penetrating microwave radiation *IEEE 1984 Ultrasonics Symp. (Dallas, TX)* ed B R Mcavoy pp 633–8
- NCCN 2015 NCCN clinical practice guidelines in oncology: prostate cancer ([www.nccn.org/professionals/physician\\_gls/pdf/prostate.pdf](http://www.nccn.org/professionals/physician_gls/pdf/prostate.pdf))
- NCCN 2014 NCCN clinical practice guidelines in oncology: prostate cancer early detection *Biopsy Technique* ([www.nccn.org/professionals/physician\\_gls/pdf/prostate\\_detection.pdf](http://www.nccn.org/professionals/physician_gls/pdf/prostate_detection.pdf))
- Nie L, Xing D and Yang S 2009 *In vivo* detection and imaging of low-density foreign body with microwave-induced thermoacoustic tomography *Med. Phys.* **36** 3429–37
- Nie L, Xing D, Zhou Q, Yang D and Guo H 2008 Microwave-induced thermoacoustic scanning CT for high-contrast and noninvasive breast cancer imaging *Med. Phys.* **35** 4026–32
- Olsen R and Lin J 1983 Acoustical imaging of a model of a human hand using pulsed microwave irradiation *Bioelectromagnetics* **4** 397–400
- Outwater E K and Montilla-Soler J L 2013 Imaging of prostate carcinoma *Cancer Control* **20** 161–76 (PMID: 23811700)
- Pachauri D, Stiles T, Purwar N, Dey P and Patch S K 2008 Transducer frequency response and impact on TPOAT signal *Photons Plus Ultrasound: Imaging and Sensing 2008: The Ninth Conf. on Biomedical Thermoacoustics, Optoacoustics and Acousto-optics* vol 6856 (San Jose, CA: SPIE)
- Parker K, Doyle M and Rubens D 2011 Imaging the elastic properties of tissue: the 20 year perspective *Phys. Med. Biol.* **56** R1–29
- Patch S, Rao N, Kelly H, Jacobsohn K and See W 2011 Specific heat capacity of freshly excised prostate specimens *Physiol. Meas.* **32** N55–64
- Patterson M, Arsenaault M, Riley C, Kolios M and Whelan W 2010 Optoacoustic imaging of an animal model of prostate cancer *SPIE BIOS Conf. on Photons Plus Ultrasound: Imaging and Sensing 2010 (San Francisco, CA)* vol 75641B
- Razansky D, Kellnberger S and Ntziachristos V 2010. Near-field radiofrequency thermoacoustic tomography with impulse excitation *Med. Phys.* **37** 4602–7 (PMID: 20964177)
- Roggenbuck M, Catenacci J, Walker R, Hanson E, Hsieh J and Patch S 2013a Thermoacoustic imaging with VHF signal generation—a new contrast mechanism for cancer imaging over large fields of view *Abdomen and Thoracic Imaging: An Engineering & Clinical Perspective* ed E L Baz, L Saba and J Suri (New York: Springer) p 523
- Roggenbuck M, Walker R, Catenacci J and Patch S 2013b Volumetric thermoacoustic imaging over large fields of view *Ultrason. Imaging* **35** 57–67
- Rooij M D, Hamoen E, Fütterer J, Barentsz J and Rovers M 2014 Accuracy of multiparametric MRI for prostate cancer detection: a meta-analysis *Am. J. Radiol.* **202** 343–51
- Salami S, Vira M, Turkbey B, Fakhoury M, Yaskiv O, Villani R, Ben-Levi E and Rastinehad A 2014 Multiparametric magnetic resonance imaging outperforms the prostate cancer prevention trial risk calculator in predicting clinically significant prostate cancer *Cancer* **120** 2876–82
- Serkova N J, Gamito E J, Jones R H, O'donnell C, Brown J L, Green S, Sullivan H, Hedlund T and Crawford E D 2008 The metabolites citrate, myo-inositol, and spermine are potential age-independent markers of prostate cancer in human expressed prostatic secretions *Prostate* **68** 620–8
- Society A C 2013 *Cancer Facts and Figures 2013* Atlanta
- Stamatakis L *et al* 2013 Accuracy of multiparametric magnetic resonance imaging in confirming eligibility for active surveillance for men with prostate cancer *Cancer* **119** 3359–66
- Su J L, Bouchard R R, Karpouk A B, Hazle J D and Emelianov S Y 2011 Photoacoustic imaging of prostate brachytherapy seeds *Biomed Opt. Express* **2** 2243–54
- Tao C, Song T, Yang W and Wu S 2006 Ultra-wideband microwave-induced thermoacoustic tomography of human tissues *IEEE Nucl. Sci. Symp. Conf. Rec.* **4** 2584–8
- Umbehre M, Bachmann L M, Held U, Kessler T M, Sulser T, Weishaupt D, Kurhanewicz J and Steurer J 2009 Combined magnetic resonance imaging and magnetic resonance spectroscopy imaging in the diagnosis of prostate cancer: a systematic review and meta-analysis *Eur. Urol.* **55** 575–90

- Wang L V and Wu H-I 2007 *Biomedical Optics: Principles and Imaging* (Hoboken, NJ: Wiley-Interscience)
- Wang L V, Zhao X, Sun H and Ku G 1999 Microwave-induced acoustic imaging of biological tissues *Rev. Sci. Instrum.* **70** 3744–8
- Wang X, Bauer D R, Witte R and Xin H 2012 Microwave-induced thermoacoustic imaging model for potential breast cancer detection *IEEE Trans. Biomed. Eng.* **59** 2782–91
- Wang X, Roberts W, Carson P, Wood D and Fowlkes B 2010 Photoacoustic tomography: a potential new tool for prostate cancer *Biomed. Opt. Express* **1** 1117–26
- Warlick C 2014 Multiparametric MRI for prostate cancer: seeing is believing cancer *Cancer* **120** 2806–9
- Xu M and Wang L 2002 Pulsed-microwave-induced thermoacoustic tomography: filtered backprojection in a circular measurement configuration *Med. Phys.* **29** 1661–9
- Yan J, Tao C and Wu S 2005 Energy transform and initial acoustic pressure distribution in microwave-induced thermoacoustic tomography *IEEE EMBS 27th Annual Conf. 2005 (Shanghai, China)* pp 1521–4
- Zukotynski K and Haider M A 2013 Imaging in prostate carcinoma *Hematol. Oncol. Clin. North Am.* **27** 1163–87